Associating ground magnetometer observations with current or voltage generators

M.D. Hartinger[1,2], Z. Xu[1,2], C.R. Clauer[1,2], Y. Yu[3], D.R. Weimer[1,2], H. Kim[4], V. Pilipenko[5], D.T. Welling[6], R. Behlke[7], A.N. Willer[7]

[1]Bradley Department of Electrical and Computer Engineering, Virginia Tech, Blacksburg, Virginia, USA.
[2]National Institute of Aerospace, Hampton, Virginia, USA.
[3]School of Space and Environment, Beihang University, Beijing, China.
[4]Center for Solar-Terrestrial Research, New Jersey Institute of Technology, Newark, New Jersey, USA.
[5]Space Research Institute, Moscow, Russia
[6]Climate and Space Sciences and Engineering Department, University of Michigan, Ann Arbor, Michigan, USA.
[7]National Space Institute, Technical University of Denmark, Denmark

Key Points:

- Conductivity and location assumptions used to interpret ground magnetic perturbations yield conflicting results
- High latitude currents associated with voltage generators may instead be associated with current generators, and vice versa
- Without better constraints on conductivity/station location relative to currents, conflicts will not be resolved

This is the author manuscript accepted for publication and has undergone full peer review but has not been through the copyediting, typesetting, pagination and proofreading process, which may lead to differences between this version and the Version of Record. Please cite this article as doi: 10.1002/2017JA024140

Corresponding author: Michael D. Hartinger, mdhartin@vt.edu

Abstract

A circuit analogy for Magnetosphere-Ionosphere current systems has two extremes for drivers of ionospheric currents: ionospheric electric fields/voltages constant while current/conductivity vary - the "voltage generator" - and current constant while electric field/conductivity vary - the "current generator". Statistical studies of ground magnetometer observations associated with dayside Transient High Latitude Current Systems (THLCS) driven by similar mechanisms find contradictory results using this paradigm: some studies associate THLCS with voltage generators, others with current generators. We argue most of this contradiction arises from two assumptions used to interpret ground magnetometer observations: (1) measurements made at fixed position relative to the THLCS field-aligned current and (2) negligible auroral precipitation contributions to ionospheric conductivity. We use observations and simulations to illustrate how these two assumptions substantially alter expectations for magnetic perturbations associated with either a current or voltage generator. Our results demonstrate that before interpreting ground magnetometer observations of THLCS in the context of current/voltage generators, the location of a ground magnetometer station relative to the THLCS field-aligned current and the location of any auroral zone conductivity enhancements need to be taken into account.

1 Introduction

1.1 The ground magnetic response during increases in solar wind dynamic pressure

Increases in solar wind dynamic pressure compress the Earth's magnetosphere, leading to transient magnetopause ripples, compressional waves, and vortical plasma flows inside the magnetopause boundary. The vortical flows in turn generate Alfvén waves that carry field-aligned currents to the ionosphere, forming Transient High Latitude Current Systems [THLCS, e.g., *Kivelson and Southwood*, 1991; *Glassmeier*, 1992a; *Araki*, 1994; *Fujita et al.*, 2003]. Such THLCS produce spatially localized field-aligned currents that can be remote sensed using ground magnetometers. For example, *Friis-Christensen et al.* [1988] used chains of ground magnetometers to associate ~10 minute, bipolar magnetic field perturbations seen at single magnetometer stations with unique, large scale vortical structures that move tailward: Traveling Convection Vortices (TCV). Later studies associated TCVs with solar wind pressure variations as well as other driving mechanisms [e.g., *Glassmeier and Heppner*, 1992b; *Sibeck et al.*, 2003].

Particularly large increases in solar wind pressure generate several transient current systems with distinct latitude and longitude dependent ground magnetic perturbations [*Araki*, 1994]. These Sudden Commencements (SC) include the Preliminary Impulse (PI) and Main Impulse (MI) response associated with the same type of current system that generates pressure-driven TCVs [*Fujita and Tanaka*, 2006]. Both TCVs and the high latitude PI/MI SC response are associated with field-aligned currents spatially localized in two dimensions, bipolar magnetic responses, and vortical patterns that move tailward [*McHenry and Clauer*, 1987; *Glassmeier*, 1992a; *Engebretson et al.*, 1999; *Fujita et al.*, 2003]. To reduce confusion and emphasize the similarity between the solar wind pressure driven current systems discussed in this study, we will simply refer to both TCV and the high-latitude PI/MI response as THLCS magnetic perturbations.

THLCS are often described using an electrical circuit analogy, with the ionosphere functioning as a load and a process in the magnetosphere functioning as a battery, or generator [e.g., *Sibeck et al.*, 1996; *Lam and Rodger*, 2004]. A process outside the ionosphere generates a potential difference that maps along magnetic field lines to the ionosphere, where it drives steady ionospheric convection and electric fields. The electric field and corresponding ionospheric potential differences can be regarded as the output voltage of the "generator," i.e., the process that initiated the electric field outside the ionosphere. If the external process driving the electric field behaves as a "voltage generator," then one expects the ionospheric electric field to remain constant while ionospheric current intensities and/or conductivities may vary. In contrast, if the external process behaves as a "current generator," one expects current intensities to remain fixed while ionospheric electric fields and/or conductivities may vary.

One can use these electrical circuit models to show that ground magnetic perturbations associated with voltage generators are proportional solely to the local Hall conductivity, whereas those associated with current generators are proportional to the ratio of Hall to Pedersen conductivities [e.g., *Sibeck et al.*, 1996]. When comparing magnetically conjugate observations - observations which lie on the same magnetic field line [*Oguti*, 1969] - the ratio of the magnitude of horizontal magnetic perturbations is given by:

$$R = \frac{BH_N}{BH_S} = \frac{\Sigma_{HN}}{\Sigma_{HS}} \tag{1}$$

$$R = \frac{BH_N}{BH_S} = \frac{\Sigma_{HN}}{\Sigma_{PN}}\frac{\Sigma_{PS}}{\Sigma_{HS}} \tag{2}$$

for voltage generators and current generators, respectively [*Lam and Rodger*, 2004]. Here, BH_N, Σ_{HN} and Σ_{PN} are for the northern hemisphere horizontal magnetic perturbation, Hall conductivity, and Pedersen conductivity, respectively, while the same quantities with the S subscript are for the southern hemisphere. Equivalent expressions to Equations 1 and 2 can be derived in time dependent situations, and these expressions also depend on ionospheric conductivities [e.g., *Lysak*, 1985, 1990].

1.2 Conflicting results from previous studies of the THLCS ground magnetic response

Previous studies have used the theoretical framework represented by Equations 1 and 2 to interpret THLCS ground magnetic perturbations. For example, *Lam and Rodger* [2004] used magnetometer data at magnetically conjugate stations to examine THLCS associated with changes in solar wind dynamic pressure. They statistically compared two groups of THLCS events: (1) equinox events with conjugate ionospheres having similar conductivities (assumed within a factor of two), (2) solstice events with conjugate ionospheres having different conductivities (assumed to differ by a factor of ten). Statistically, *Lam and Rodger* [2004] found magnetic perturbation amplitudes were similar in both hemispheres regardless of season. Using measured magnetic field amplitudes and assumed conductivities, they concluded their results were consistent with Equation 2 for current generators.

In another example, *Shinbori et al.* [2012] conducted a statistical study of north-south magnetic perturbations (BX) during 3535 THLCS events at northern hemisphere stations. After using a normalization factor to remove BX dependence on the size of the solar wind dynamic pressure increase, *Shinbori et al.* [2012] examined the BX seasonal variation at different latitudes. Auroral zone (represented by a station at 61.8 degrees) and high latitude (represented by a station at 66.3 degrees) BX were observed to vary with season. For example, in the auroral zone, the summer and winter values of normalized BX differ by roughly a factor of 1-3, depending on MLT (Figure 6 in *Shinbori et al.* [2012]). *Shinbori et al.* [2012] used these seasonal variations to associate the auroral zone/high latitude THLCS with voltage generators, arguing the seasonal dependence in perturbation amplitude corresponded to seasonal variations in ionospheric conductivities.

The theory used in *Lam and Rodger* [2004] and *Shinbori et al.* [2012] permits only the current or voltage generator interpretation, not both, since the driver is the same in both studies. The analysis used in both studies allows for three possible outcomes:

1. Voltage generator: Different conductivities in different seasons or hemispheres yield different magnetic perturbation amplitudes.

2. Current generator: Different conductivities in different seasons or hemispheres yield similar magnetic perturbation amplitudes.
3. Inconclusive: Similar conductivities in different seasons or hemispheres yield similar magnetic perturbation amplitudes, making it impossible to differentiate between current and voltage generators.

Both studies argued that conductivities differed sufficiently to eliminate the third possibility, and, despite carefully constructed methodologies and justified assumptions, they arrived at opposite conclusions: *Lam and Rodger* [2004] associates solar wind pressure driven THLCS with current generators, *Shinbori et al.* [2012] with voltage generators.

Our motivation for this study is to reconcile the contrasting results of *Lam and Rodger* [2004] and *Shinbori et al.* [2012] by examining the effect of two assumptions used to interpret THLCS ground magnetic perturbations: observations at fixed position relative to the THLCS field-aligned current and negligible auroral precipitation contributions to ionospheric conductivity. In particular, if the assumption for the measurement location relative to the THLCS field-aligned current is not well constrained (e.g., variation between hemisphere or season not accounted for), the comparison of perturbation amplitudes will be affected. If the conductivity assumptions are not well constrained, the postulated differences in perturbation amplitudes may be inaccurate. Both assumptions affect the ability to discriminate between (1), (2), and (3) above. In the remainder of this paper, we use observations and numerical simulations of a THLCS event to examine the effect of these assumptions on the interpretation of THLCS ground magnetic perturbation observations.

2 Case Study on 19 Jan 2013: Observations and SWMF simulations

We examine a THLCS event reported by *Kim et al.* [2015] that occurred on 19 Jan 2013 at approximately 1730 UT and was driven by the arrival of an interplanetary shock. *Kim et al.* [2015] compared ground magnetic perturbation observations in both hemispheres; in particular, they compared observations from a north-south chain of magnetometers in Greenland - operated by the National Space Institute at the Technical University of Denmark (DTU Space) - as well as a north-south chain of Autonomous Adaptive Low-Power Instrument Platform (AAL-PIP) Antarctic stations [*Clauer et al.*, 2014]. In this study, we will also use two ground magnetometer stations operated by the British Antarctic Survey, B14 (m81-338) and B16 (m83-347), and one Automated Geophysical Observatory station, AGO3 [*Rosenberg and Doolittle*, 1994]. The magnetic coordinates of these stations are shown in Table 1, based on IGRF calculations appropriate for 19 Jan 2013. By design, many southern hemisphere stations lie on the same or nearly the same IGRF field line as a northern hemisphere station [*Clauer et al.*, 2014].

Several features of this event make it a useful case study to examine how assumptions for measurement location and auroral zone conductivity affect the interpretation of ground magnetic perturbation observations. As shown in Table 1, there are multiple stations that are nominally magnetically conjugate. The event occurred near solstice, when conductivity differences should be large between the northern and southern hemisphere; this presents an opportunity to test the current/voltage generator hypotheses by comparing conjugate observations, since the R value associated with voltage generators ought to differ substantially from R associated with current generators (Equations 1 and 2) if the conductivities in each hemisphere differ substantially [*Lam and Rodger*, 2004]. Finally, the stations span a wide range of latitudes that include the nominal auroral oval.

2.1 Overview of Space Weather Modeling Framework Simulations

We compare observations with a series of Space Weather Modeling Framework (SWMF) simulations. SWMF is a scheme for coupling many models designed to simulate different physics domains [*Tóth et al.*, 2005]. For this study, we use two SWMF models,

Table 1. Ground magnetometer locations in corrected geomagnetic coordinates. These coordinates were obtained using the NASA Virtual Ionosphere, Thermosphere, Mesosphere Observatory via the online OMNI-Web interface by specifying each station's geographic position, the 2013 version of the IGRF model, and an altitude of 0 km. These coordinates may differ slightly from those reported elsewhere when using a different version of IGRF.

N Hemisphere	Lat	Lon	S Hemisphere	Lat	Lon
THL	84.40	27.35			
SVS	82.67	31.12			
KUV	80.36	40.20			
UPN	78.57	38.64			
UMQ	75.99	41.16	PG1	-77.05	37.50
GDH	74.82	38.10	PG2	-75.32	39.16
ATU	73.53	37.05	PG3	-73.59	36.72
STF	72.14	39.92	AGO3	-72.07	41.00
SKT	70.93	36.40			
GHB	69.49	37.09	B16 (m83-347)	-68.71	30.48
FHB	66.91	38.40	B14 (m81-338)	-66.67	29.15
NAQ	65.23	42.59			

a single fluid version of BATS-R-US for the Earth's magnetosphere [*Powell et al.*, 1999] and the Ridley Ionosphere Model [RIM, *Ridley and Liemohn*, 2002; *Ridley et al.*, 2004]. SWMF couples these two models by (1) mapping field-aligned currents from the inner boundary of BATS-R-US to the ionosphere/RIM, (2) generating a conductivity pattern, (3) solving for the electric potential in RIM, (4) mapping the electric potential to the inner boundary of BATS-R-US, (5) using the electric potential to calculate electric fields and velocities in BATS-R-US (see *Ridley et al.* [2004] for more details).

Both BATS-R-US and RIM include options to compute ground magnetic perturbations associated with ionospheric and magnetospheric currents [*Yu and Ridley*, 2008; *Yu et al.*, 2010]. In particular, currents in the coupled BATS-R-US/RIM SWMF simulation are divided into four categories: Hall currents extracted from RIM, Pedersen currents extracted from RIM, field-aligned currents extracted from the gap between the inner boundary of BATS-R-US and RIM, and all magnetospheric currents in BATS-R-US. Each type of current is separately used to compute the ground-magnetic perturbation at specific locations using the Biot-Savart Law before combining the contributions from all currents together [*Yu et al.*, 2010]. For the purpose of this study, we extract ground magnetic perturbations at locations corresponding to the magnetometer stations in Table 1. These techniques have successfully been used in previous studies comparing BATS-R-US/RIM SWMF simulations with observed ground magnetic perturbations [e.g., *Yu and Ridley*, 2009, 2011; *Pulkkinen et al.*, 2013].

We conducted four SWMF simulations with identical driving conditions but different ionospheric conductivities and dipole tilt values. Table 2 summarizes the key differences between the four simulations used for this study. We note that for all simulations, we compared SWMF virtual satellite and magnetometer output to observations at several locations - including THEMIS-A at the subsolar point (not shown) - and found that applying an 11 minute time shift to all simulation output provided the best match to the data. Since the same shift worked at a variety of positions, this is likely due to timing errors in propagating the solar wind observations from the upstream monitor to the outer boundary of the simulation domain. Hereafter, we apply this time shift to all simulation output and note that it has no effect on any of the conclusions of this study - it simply makes it easier

Table 2. Overview of SWMF simulations

Name	RIM Conductivity Model	Dipole Tilt
Uniform	Hall=Pedersen=5 mho everywhere	Yes
Solar	Conductivity varies according to solar zenith angle	Yes
Auroral	Conductivity varies according to solar zenith angle and auroral precipitation	Yes
Uniform, No Tilt	Hall=Pedersen=5 mho everywhere	No

to compare the virtual ground magnetometer data to observations. We also note that solar wind variations in BATSRUS are propagated from the upstream boundary towards the Earth as planar fronts, and that the orientation of these fronts may not always reflect observations [*Weimer et al.*, 2002; *Oliveira and Raeder*, 2014, 2015]. For this reason, and due to lack of observational constraints on ionospheric conductivity, we do not expect exact quantitative agreement between observations and simulations. However, this is not needed for this study. The sole purpose of the simulations is to illustrate the points in the previous section by examining how ionospheric conductivity and magnetic field topology affect ground magnetic observations in similar driving conditions.

In the first simulation, referred to hereafter as "Uniform," we used a realistic dipole tilt value and uniform ionospheric conductivities, where the Hall and Pedersen conductivities are 5 mho everywhere on the RIM grid. In the second simulation, hereafter referred to as "Solar," we use the same tilt value but with more realistic conductivity patterns that include the effect of asymmetric solar illumination. In this simulation, conductivities are computing using (1) solar EUV (represented by a constant F10.7 flux), (2) sunlight scattering across the terminator, and (3) a small contribution to the conductivity from nightside "starlight" conductance. This simulation thus captures the large noon-midnight asymmetry expected for ionospheric conductivity as well as the northern-southern hemisphere asymmetry expected for near-solstice conditions on 19 Jan. In the third simulation, hereafter referred to as "Auroral," we use the same configuration as the second, but we also include auroral oval conductance contributions. In particular, the contribution to the ionospheric conductance expected from auroral oval precipitation is represented using an empirical relationship between the simulated field-aligned currents and the conductance [*Ridley et al.*, 2004]. Finally, in the fourth simulation, referred to as "Uniform, No Tilt," we used the same conductivity pattern as the Uniform simulation, but we removed the dipole tilt - i.e., the Earth's rotation axis is aligned with the dipole axis.

Figure 1 compares the Hall conductivity profiles we used in each of the simulations in the North (top) and South (bottom) hemisphere at 1734 UT. In each plot, the conductivity is shown in color on a polar projection of the northern and southern hemispheres (0 to 30 degrees latitude from each pole are shown), with the noon region at the top, From left to right, the conductivity from the Uniform simulation (same as simulation with no tilt), Solar simulation, and Auroral simulation. Positions of ground magnetometer stations at 1734 UT are indicated by white crosses.

In all simulations, we use the same solar wind driving conditions shown in the top three panels of Figure 2. These are based on observations during the 19 Jan 2013 17:30 UT event reported by *Kim et al.* [2015]. From top to bottom, these panels show the interplanetary magnetic field (IMF) in GSM coordinates, solar wind velocity in GSM coordinates, and solar wind dynamic pressure, all taken from a virtual satellite at GSM position r=[25,0,0] R_E. The most prominent feature in the solar wind data is a step-like change in

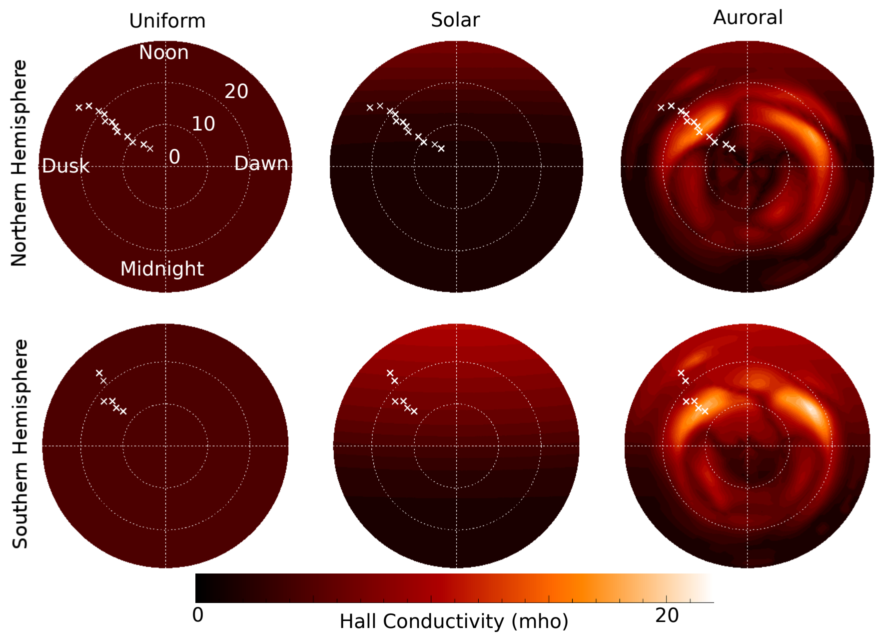

Figure 1. Conductivity profiles used in SWMF simulations at 1734 UT. The top/bottom row is for the northern/southern hemisphere. Each column is for a different simulation. In each panel, Hall conductivity is shown in color from 0 to 30 degrees from the pole, with noon at the top and dusk at the right. White crosses indicate the location of stations in Table 1.

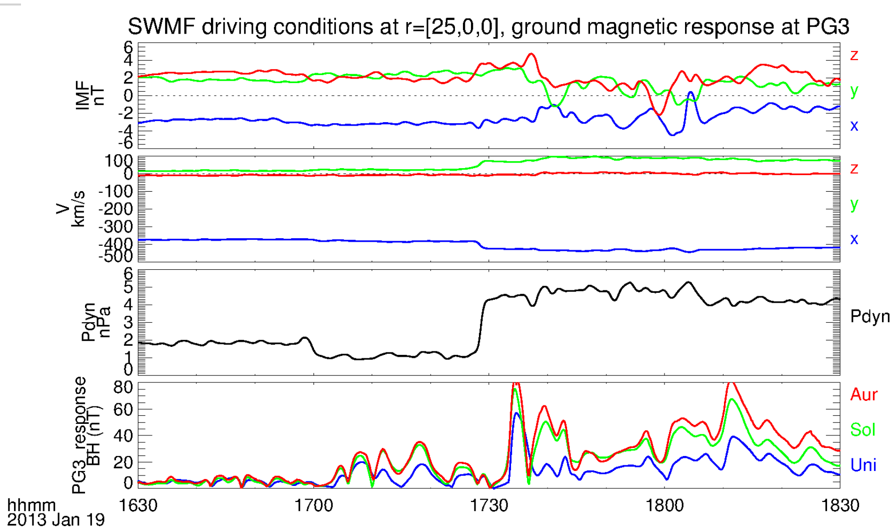

Figure 2. The top three panels are for the solar wind driving conditions used in all simulations. sampled at r=[25,0,0] GSM coordinates. From top to bottom, the three components of the interplanetary magnetic field, the three components of the solar wind velocity (both in GSM), and the solar wind dynamic pressure. The bottom panel is for the horizontal magnetic perturbation ($BH = \sqrt{BX^2 + BY^2}$), at the PG3 virtual magnetometer in Uniform (blue line), Solar (green line), and Auroral (red line) simulations.

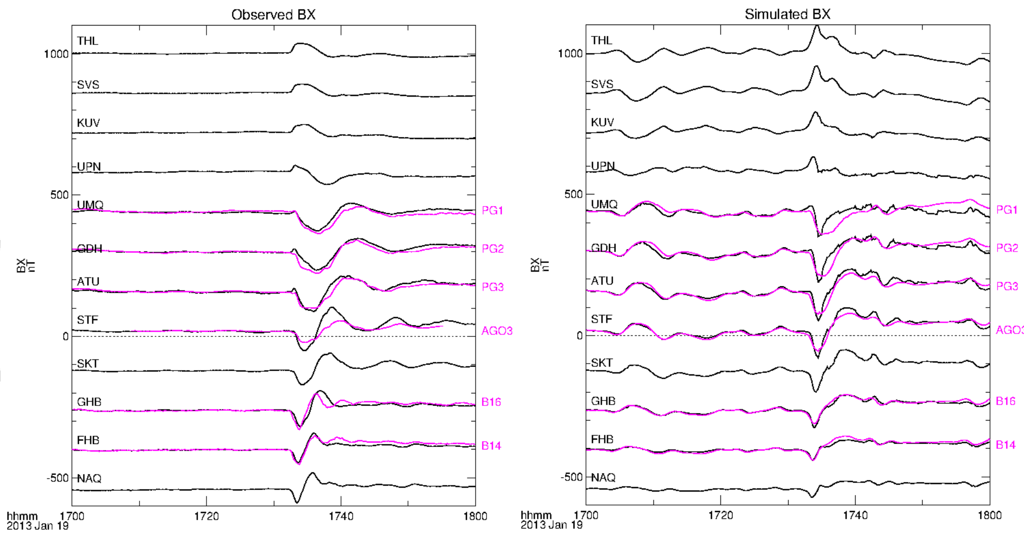

Figure 3. Comparisons between simulated and observed north-south magnetic perturbations. Left) Observed North-south magnetic perturbation (BX) from magnetometers in the northern hemisphere (black lines) and their southern hemisphere counterparts (pink lines). Right) The same as at left, but for virtual magnetometers in the Auroral simulation.

dynamic pressure just before 1730 UT. This signals the arrival of an interplanetary shock and a compression of the magnetosphere. The bottom panel shows the horizontal magnetic perturbation ($BH = \sqrt{BX^2 + BY^2}$, X indicates the north-south magnetic direction, Z indicates the vertical direction, and Y completes the right-hand orthogonal set pointing approximately eastward), at the PG3 virtual magnetometer in Uniform (blue line), Solar (green line), and Auroral (red line) simulations. All simulations see a sharp increase in BH after the shock impacts the dayside magnetosphere, but there are significant differences in the amplitude of BH; these differences will be discussed in section 2.2.

The simulation domain is GSM x from -96 to 32 R_E, y from -64 to 64 R_E, and z from -64 to 64 R_E, with the inner boundary of BATS-R-US a sphere at r=2.5 R_E. The Cartesian BATS-R-US grid has a variable cell size. The grid cells have widths of 1/8 R_E in the region from $-16 \leq x \leq 16$, $-16 \leq y \leq 16$, and $-16 \leq z \leq 16$, with gradually increasing cell sizes and, thus, decreasing resolution outside of this region. To better resolve small scale current systems near the inner boundary of BATS-R-US, we also added a spherical shell of higher resolution 1/16 R_E grid cells between 2.5 (inner boundary) and 4.0 R_E. As in previous work using SWMF [*Hartinger et al.*, 2014, 2015], we tested how numerical diffusion affects our results by using a variety of simulations with identical configurations, apart from the grid. We found that variations in the grid cell size had no effect on the large scale THLCS properties or the conclusions of our study.

2.2 Simulation Results and Comparisons with Observations

Figure 3 shows comparisons between the measured and simulated north-south magnetic perturbations (BX) for the 19 Jan 2013 event. The left panel is for a stackplot containing all northern hemisphere magnetometer observations used in this study (black lines, coordinates given in left part of Table 1), ordered from highest magnetic latitude at the top to lowest at the bottom, and their respective IGRF conjugate stations in the southern hemisphere (pink lines, coordinates given in right part of Table 1). All stations shown are near the 15 MLT meridian at the time of shock arrival, though the two BAS stations

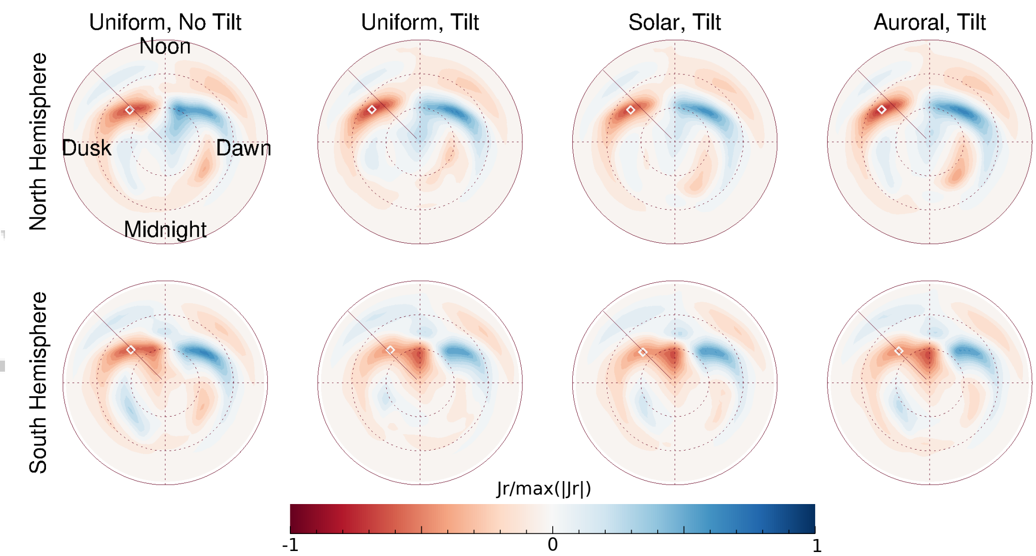

Figure 4. Global current systems at 1734 UT. Radial current (color) in the northern hemisphere (top row) and southern hemisphere (bottom row) normalized to the maximum radial current intensity (across all simulations/hemispheres), with each column for a different simulation. Each panel uses the same perspective as in Figure 1, a black line indicates 15 MLT, and a white diamond indicates the location of maximum current intensity post-noon.

are separated by 5-10 degrees longitude from the rest of the chain. Several features are seen that are consistent with expectations for the dusk sector high-latitude magnetic response driven by large dynamic pressure increases: bipolar signature, negative perturbation followed by positive at auroral latitudes (referred to as the Preliminary Impulse and Main Impulse, or collectively as a TCV, see section 1.1), positive followed by negative at higher latitudes [*Araki*, 1994; *Fujita et al.*, 2003; *Yu and Ridley*, 2009, 2011]. Comparing the black lines to the pink, it is also clear that the southern hemisphere response is very similar to the northern hemisphere response when comparing both amplitude and timing.

The right part of Figure 3 is for virtual magnetometer results from the Auroral simulation (Table 2). Similar features are seen as on the left - for example, the bipolar signature (clearest at latitudes below 74 degrees). We also see significant agreement between the northern and southern hemispheres. We attribute differences between observations and simulations mainly to our inability to observationally constrain ionospheric conductivity near the auroral oval. Future simulation studies could improve these results with better observational constraints on the conductivity and/or more sophisticated models of auroral precipitation [e.g., *Yu et al.*, 2016]; for the present study, an exact match is not needed as our sole purpose is to qualitatively illustrate how ionospheric conductivity and magnetic field topology affect ground magnetic observations.

Figure 4 explores the effect of ionospheric conductivity on the global THLCS pattern, examining currents at 1734 UT. Each panel in the top two rows shows the radial (out of the RIM grid, approximately parallel to magnetic field in southern hemisphere and anti-parallel in north) current as color; the black line indicates the 15 MLT meridian, and the white diamond indicates the location of maximum THLCS field aligned current intensity post-noon. The top row is for the polar projection of northern hemisphere currents (0 to 30 degrees magnetic latitude from the magnetic pole) while the second row is for the southern hemisphere; for ease of comparison between north and south, the currents are

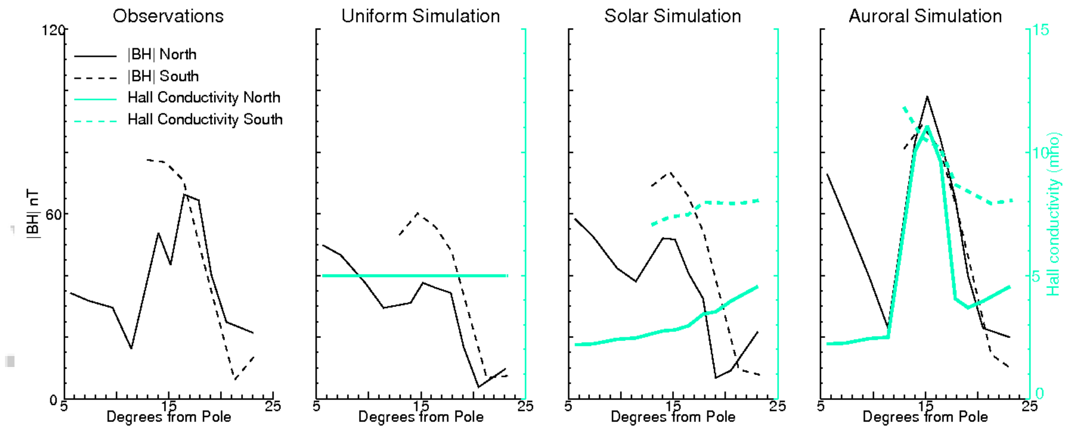

Figure 5. Each panel shows the horizontal magnetic perturbation at magnetometers near 15 MLT in the northern hemisphere (solid black line) and southern hemisphere (dashed black line) at 1735 UT. The left panel is for observations, the right three panels are for different simulations. For simulations, the local Hall conductivity is also shown at each northern hemisphere virtual magnetometer (solid cyan line) and southern hemisphere virtual magnetometer (dashed cyan line).

displayed from the perspective of an observer above the north magnetic pole (i.e., when observing the southern hemisphere currents, one is looking through the Earth). Finally, each column is for a different simulation: from left to right, Uniform No Tilt, Uniform (with tilt), Solar (with tilt), Auroral (with tilt).

As shown in the top row (northern hemisphere), all four simulations capture the large scale THLCS expected to accompany the initial arrival of interplanetary shocks; spatially localized currents into the ionosphere (red) at dusk and out (blue) at dawn, in both hemispheres [*Araki*, 1994; *Fujita et al.*, 2003; *Yu and Ridley*, 2009]. As expected, the second row (southern hemisphere) also sees this pattern, somewhat distorted - as indicated by the outward (blue) current region extending past noon - but qualitatively similar. Comparing the location of the white diamond in the left panel of the top row to the rest of the panels in the top row, it is clear that introducing a dipole tilt breaks some of the symmetry between the northern and southern hemisphere. For example, in columns 2-4, the white diamond in the northern hemisphere (top row) is at a different longitude than in the southern hemisphere (bottom row). As we will show in the next figure, this breaking of symmetry affects ground magnetic perturbation comparisons between the northern and southern hemispheres.

Having examined the global THLCS pattern, we return to the simulated and observed ground magnetometer observations near the 15 MLT meridian. Figure 5 examines how BH varies between different hemispheres and simulations, as a function of distance from the north or south pole. We chose to calculate BH at the same time for all stations, 1735 UT, which is roughly the time the maximum BH was observed across all stations and simulations. We tried different times, as well as using a different time for each station and component (as was done in *Lam and Rodger* [2004]) and found qualitatively similar results, though with less clear trends in the case of the observations. One notable trend in these tests was that $|BX|$ tended to be more similar between the northern and southern hemispheres - when compared to BH and $|BY|$ - as indicated by the very similar northern/southern hemisphere observations shown in Figure 3.

Table 3. Amplitude and Conductivity Ratios from Equations 1 and 2 at Different Station Pairs: Auroral simulation at 1735 UT

Station Pair	$\frac{BHN}{BHS}$	$\frac{\Sigma_{HN}}{\Sigma_{HS}}$	$\frac{\Sigma_{HN}}{\Sigma_{PN}}\frac{\Sigma_{PS}}{\Sigma_{HS}}$
UMQ-PG1	1.0	0.85	1.2
GDH-PG2	1.1	1.0	1.3
ATU-PG3	1.0	0.94	1.3
STF-AGO3	1.0	0.47	1.1
GHB-B16	1.6	0.50	1.0
FHB-B14	2.1	0.57	1.0

The left panel of Figure 5 shows BH observations for the northern (solid black line) and southern hemisphere stations (dashed black line) listed in Table 1. A clear maximum is seen in the northern hemisphere near 17-18 degrees, and BH is within a factor of two in the northern and southern hemisphere at all latitudes where data are available. The next three panels are for simulated magnetometer data at the same locations as the observations; only data from simulations with realistic tilt values are shown for data-model comparisons. In each panel, BH is shown as before with additional cyan lines added for the local Hall conductivity near each station. In the Uniform simulation (second panel from left), BH is larger in the southern hemisphere at most latitudes despite the Hall and Pedersen conductivities being equal everywhere. As shown in Figure 4, this is because the northern and southern hemisphere stations are not located at the same position relative to the THLCS field-aligned current when a realistic dipole tilt is used.

In the simulation with asymmetric conductivities due to solar illumination (third panel from left), BH is again larger in the southern hemisphere at most latitudes, though the difference between north and south is not as large as it ought to be to satisfy the voltage generator hypothesis (Equation 1). Indeed, the ratio of BH values in the northern and southern hemispheres near the maximum of BH at 15 degrees is smaller in the Solar conductivity simulation when compared to the Uniform conductivity simulation, despite the presence of a large Hall conductivity asymmetry (solid and dashed cyan lines). For THLCS associated with voltage generators, the opposite trend should have occurred: larger BH ratios in the presence of larger conductivity ratios.

The right panel of Figure 5 is for the simulation with conductivity contributions from both solar illumination and auroral precipitation; note the presence of the large, local peak in Hall conductivity near 15 degrees (solid cyan line). Also note that, unlike in other simulations, BH is approximately the same in both hemispheres at most latitudes. The contributions from auroral precipitation (as parameterized by the RIM and BATS-R-US models) to overall conductivities reduces the north-south BH asymmetry seen in other simulations.

Table 3 displays the ratios in Equations 1 and 2 used by *Lam and Rodger* [2004] to test the voltage and current generator hypotheses, calculated for the Auroral simulation. The first column shows the station pairs used to calculate the ratio. The second, third, and fourth columns are for the ratios in Equations 1 and 2. As shown in Figure 5, auroral precipitation is a major contributor to the overall conductivity. This is reflected in the the third column of Table 3, where the northern and southern hemisphere Hall conductivities are within roughly a factor of two despite the fact that for most station pairs, one station is in darkness while the other is in sunlight.

Inspecting columns 2-4 of Table 3, it is hard to decide whether the simulation results are consistent with the current or voltage generator hypothesis. Most stations are near the auroral oval, where conductivity ratios are too close to 1 to differentiate between the two hypotheses. This illustrates how auroral zone conductivities can reduce the size of hemispheric and seasonal differences in ionospheric conductivity, making ionospheric conductivity effects on THLCS magnetic perturbation amplitudes comparable to other effects, such as relative distance to THLCS field-aligned currents. If the conductivity profile used in this simulation was not known and one were to interpret the second column of Table 3 using an assumption similar to *Lam and Rodger* [2004], one would associate these ratios with a current generator. If one instead assumed substantial auroral precipitation contributions to conductivity, it would not be possible to differentiate between the current and voltage generator cases.

For brevity sake, we do not include tables for the other simulations since most of the information is already shown in Figure 5. However, we note that in all simulations and for all station-pairs, the ratio $\frac{\Sigma_{HN}}{\Sigma_{PN}}\frac{\Sigma_{PS}}{\Sigma_{HS}}$ is between 1.0 and 1.3, showing significantly less variation than $\frac{\Sigma_{HN}}{\Sigma_{HS}}$. This further shows that neither Equation 1 for voltage generators nor Equation 2 for current generators describe the simulation results exactly, since BH ratios match neither conductivity ratio in all cases. This is most easily seen when examining results in the Uniform simulation, second panel from the left in Figure 5; despite the fact that all conductivity ratios are 1.0 everywhere, the BH ratio varies between 0.56 and 1.3, with the variability likely caused by varying distances relative to the THLCS field-aligned current.

3 Discussion and Summary

A circuit analogy for Magnetosphere-Ionosphere current systems has two extremes for drivers of ionospheric currents: ionospheric electric fields/voltages constant while current/conductivity vary - the “voltage generator” - and current constant while electric field/conductivity vary - the “current generator”. This theory permits only one interpretation for similar driving conditions, yet interpretations differ in past studies. In particular, *Lam and Rodger* [2004] and *Shinbori et al.* [2012] both statistically examined ground magnetometer observations associated with dayside THLCS driven by solar wind pressure variations. Despite the fact that both studies carefully constructed their respective methodologies and justified their assumptions, *Lam and Rodger* [2004] associated THLCS with current generators while *Shinbori et al.* [2012] associated THLCS with voltage generators. This apparent contradiction motivated the present study, where we have examined the effects of two assumptions used by *Lam and Rodger* [2004] and *Shinbori et al.* [2012] on the interpretation of ground magnetic perturbations: (1) measurements are taken at the same location relative to the THLCS field-aligned current, (2) negligible auroral precipitation contributions to ionospheric conductivity.

We used numerical simulations and observations of a THLCS event to demonstrate how shifting measurement locations relative to the location of peak THLCS current intensity contributes to hemispheric differences in BH. To place our case study results in context, we now estimate the typical ratio of BH for two stations in opposite hemispheres using the THLCS model of *Glassmeier and Heppner* [1992b] (Equation 9 in their Appendix):

$$\frac{BH_1}{BH_2} = \frac{r_1((\sigma + h)^2 + r_2^2)^{\frac{3}{2}}}{r_2((\sigma + h)^2 + r_1^2)^{\frac{3}{2}}} \tag{3}$$

where BH_1 and BH_2 are the horizontal magnetic perturbation magnitudes at each station, r_1 and r_2 are the horizontal distances from each station to the center of the field-aligned current, h is the height of the ionosphere, and σ sets the width of the current system. *Glassmeier and Heppner* [1992b] assumed $h = 110$ km and $\sigma = 100$ km to most closely match observations of THLCS ground magnetic perturbations generated by solar wind pressure variations. At 70 degrees magnetic latitude, typical distortions in magnetic field topology are on the order of two degrees latitude and 20-30 degrees longitude [*Ganushk-*

ina et al., 2013], corresponding to distances of roughly 200 km. Assuming $r_1 = 200$ km and $r_2 = 400$ km, $\frac{BH_1}{BH_2} = 1.89$. This is consistent with hemispheric differences found in our case study results (Figure 5, second panel from left) and suggests that for most THLCS events, if the size of conductivity differences between hemispheres is a factor of two or less, incorrect assumptions for measurement location relative to THLCS - e.g., due to distorted magnetic field topologies - will affect the association of ground magnetic perturbations with voltage or current generators. Seasonal motion of THLCS field-aligned currents relative to ground stations may also affect the interpretation of BH observations if it is not accounted for, since the location of the peak THLCS field-aligned current intensity coincides with the equatorward edge of the auroral oval [*Moretto and Yahnin*, 1998] and this location moves several degrees poleward in summer compared to winter [*Newell and Meng*, 1989]. Thus, both hemispheric comparisons [e.g., *Lam and Rodger*, 2004] and analysis of seasonal variations in a single hemisphere [e.g., *Shinbori et al.*, 2012] are affected by assumptions for measurement location relative to THLCS.

Consistent with previous statistical analysis of THLCS [*Sibeck et al.*, 1996], our simulations and observations also demonstrate how implicit or explicit assumptions for conductivities near auroral latitudes are critical to the interpretation of BH: different conductivity assumptions lead to different conclusions for similar magnetometer observations (e.g., Table 3 and related discussion). The explicit assumption of *Lam and Rodger* [2004] that conductivities differ by at least a factor of 10 when one station is in darkness and the other light is central to their finding that dayside THLCS are associated with current generators. If *Lam and Rodger* [2004] had instead assumed factor of two auroral zone conductivity differences between the sunlit and dark hemisphere, their statistical results would not have differentiated between current and voltage generators. *Shinbori et al.* [2012] found that typical summer/winter ratios in magnetic perturbation amplitude were variable but on the order of 1-3 (e.g., taking the absolute value of the data shown in Figures 6, 7, and 8 in that study for high latitude stations). Arguing the seasonal dependence in perturbation amplitude corresponded to seasonal variations in ionospheric conductivities, they associated their observations with voltage generators. If *Shinbori et al.* [2012] had instead assumed conductivities vary by a factor of 10 between summer and winter, they may have associated their observations with current generators as in *Lam and Rodger* [2004]. This discussion is not a criticism of the specific conductivity assumptions of *Lam and Rodger* [2004] or *Shinbori et al.* [2012], as there are few observational constraints on conductivity in the auroral zone; many assumptions are required to estimate conductivities using in situ particle measurements (e.g., *Hardy et al.* [1987]) or ground-based radars (e.g., *Ahn et al.* [1998]), and these observations are sparse and may not agree with each other. Nevertheless, these results suggest that progress will not be made on the interpretation of ground magnetometer observations in the context of current or voltage generators without better constraints on ionospheric conductivity.

In this study we demonstrated how location and conductivity assumptions, by themselves, can account for the apparent discrepancy between *Lam and Rodger* [2004] and *Shinbori et al.* [2012]. However, other effects may contribute. For example, large auroral zone conductivity gradients can affect perturbation amplitudes and polarizations, and these effects are not captured in Equations 1 and 2 that assume uniform conductivity [*Kamide and Matsushita*, 1979; *Glassmeier*, 1984; *Glassmeier and Junginger*, 1987; *Kosch et al.*, 2001]. However, these effects would vary from event to event depending on a number of factors (electric field polarization, sharpness and direction of gradient, spatial scale of current system) and occur over a limited latitudinal range near the strongest gradients. Thus, they cannot explain the systematic differences between *Lam and Rodger* [2004] and *Shinbori et al.* [2012], as both studies examined a wide latitudinal and longitudinal range and a large number of events. It is also possible the timescales for THLCS are not long enough to be regarded as static as assumed by Equations 1 and 2, and different equations/predictions for ground signals appropriate for time varying currents are needed [e.g., *Lysak*, 1985, 1990]. However, these expressions also depend on ionospheric conductivity and location relative to THLCS, rendering tests of these expressions susceptible to the same effects discussed in the present study.

Our results demonstrate that before interpreting ground magnetometer observations of THLCS in the context of current/voltage generators, the location of a ground magnetometer station relative to both the THLCS field-aligned current and auroral zone conductivity enhancements need to be taken into account. Though this may be trivial to implement in a model, it is difficult in most observational studies due to the lack of constraints on ionospheric conductivity and current system positions. Future observational studies could use dense north-south chains of magnetometers spanning a wide range of latitudes near the auroral oval - ideally with conjugate pairs in the opposite hemisphere [*Engebretson et al.*, 1999; *Kim et al.*, 2013, 2015] - to identify the location of the THLCS field-aligned current, its width in latitude, and its amplitude variation with latitude [*Clauer and Petrov*, 2002]. If a wide enough range of latitudes is considered, such data could be used to better constrain current system position. They could also be used to account for auroral zone conductivity enhancements by comparing seasonal and/or hemispheric variations in BH seen near the peak field-aligned current intensity with locations further way, since those locations ought to be at different positions relative to auroral zone conductivity enhancements [*Moretto and Yahnin*, 1998]. Finally, future studies could focus on events where measurements from low-Earth orbiting spacecraft or ground-based radars are available to constrain auroral conductances.

Acknowledgments

M.D. Hartinger was supported by NSF grants AGS-1049403 and PLR-1543364. V. Pilipenko was supported by NSF AGS-1264146. We acknowledge high-performance computing support from Yellowstone (ark:/85065/d7wd3xhc) provided by NCAR's Computational and Information Systems Laboratory, sponsored by the National Science Foundation. This work was carried out using the SWMF/BATS-R-US tools developed at The University of Michigan Center for Space Environment Modeling (CSEM). Magnetometer observations and simulation output files are available upon request from the corresponding author (M.D. Hartinger, mdhartin@vt.edu). Most ground magnetometer measurements and SPEDAS software for plotting can be obtained from the THEMIS website (http://themis.ssl.berkeley.edu/index.shtml). AGO and BAS magnetometer data are available upon request from NJIT and BAS. The authors thank Andrew Gerrard (PI, NJIT, under NSF grant PLR-1443507) for providing fluxgate magnetometer data from the AGO station. We thank the British Antarctic Survey for providing the low-power magnetometer data (PI Mervyn Freeman) from B14 (m81-338) and B16 (m83-347). We thank the National Space Institute at the Technical University of Denmark (DTU Space) for providing magnetometer data from the Greenland Magnetometer Array. We thank the NASA Space Science Data facility for use of Virtual Ionosphere, Thermosphere, Mesosphere Observatory models via the OMNIWeb interface. M.D. Hartinger thanks Mark Engebretson, Jennifer Posch, and Aaron Ridley for informative discussions.

References

Ahn, B.H., A.D. Richmond, Y. Kamide, H.W. Kroehl, B.A. Emery, O. de la Beaujardiere, and S.-I. Akasofu (1998), An ionospheric conductance model based on ground magnetic disturbance data, *Journal of Geophysical Research*, *103*, 14769-14780, doi:10.1029/97JA03088.

Araki, T. (1994), A Physical model of the geomagnetic sudden commencement, *Washington DC American Geophysical Union Geophysical Monograph Series*, *81*, 183-200, doi:10.1029/GM081p0183.

Clauer, C.R. and V.G. Petrov (2002), A statistical investigation of traveling convection vortices observed by the west coast Greenland magnetometer chain, *Journal of Geophysical Research (Space Physics)*, *107*, doi:10.1029/2001JA000228.

Clauer, C.R., H. Kim, K. Deshpande, Z. Xu, D. Weimer, S. Musko, G. Crowley, C. Fish, R. Nealy, T.E. Humphreys, J.A. Bhatti, and A.J. Ridley (2014), An autonomous adaptive low-power instrument platform (AAL-PIP) for remote high-latitude geospace data collection, *Geoscientific Instrumentation, Methods and Data Systems*, *3*, 211-227, doi:10.5194/gi-3-211-2014.

Engebretson, M.J., D.L. Murr, W.J. Hughes, H. Lühr, T. Moretto, J.L. Posch, A.T. Weatherwax, T.J. Rosenberg, C.G. Maclennan, L.J. Lanzerotti, F. Marcucci, S. Dennis, G. Burns, J. Bitterly, and M. Bitterly (1999), A multipoint determination of the propagation velocity of a sudden commencement across the polar ionosphere, *Journal of Geophysical Research (Space Physics)*, *104*, 22433-22452, doi:10.1029/1999JA900237.

Friis-Christensen, E., S. Vennerstrom, M.A. McHenry, and C.R. Clauer (1988), Ionospheric traveling convection vortices observed near the polar cleft - A triggered response to sudden changes in the solar wind, *Geophysical Research Letters*, *15*, 253-256, doi:10.1029/GL015i003p00253.

Fujita, S., T. Tanaka, T. Kikuchi, K. Fujimoto, and M. Itonaga (2003), A numerical simulation of the geomagnetic sudden commencement: 2. Plasma processes in the main impulse, *Journal of Geophysical Research (Space Physics)*, *108*, doi:10.1029/2002JA009763.

Fujita, S., and T. Tanaka (2006), Magnetospheric Plasma Processes During a Sudden Commencement Revealed From a Global MHD Simulation, *Washington DC American Geophysical Union Geophysical Monograph Series*, *169*, 31.

Ganushkina, N.Y., M.V. Kubyshkina, N. Partamies, and E. Tanskanen (2013), Interhemispheric magnetic conjugacy, *Journal of Geophysical Research (Space Physics)*, *118*, 1049-1061, doi:10.1002/jgra.50137.

Glassmeier, K.-H. (1984), On the influence of ionospheres with non-uniform conductivity distribution on hydromagnetic waves, *Journal of Geophysics Zeitschrift Geophysik*, *54*, 125-137.

Glassmeier, K.-H. and H. Junginger (1987), Concerning the ionospheric modification of magnetospheric hydromagnetic waves - Case studies, *Journal of Geophysical Research (Space Physics)*, *92*, doi:10.1029/JA092iA11p12213.

Glassmeier, K.-H. (1992a), Traveling magnetospheric convection twin-vortices - Observations and theory, *Annales Geophysicae*, *10*, 547-565.

Glassmeier, K.-H. and C. Heppner (1992b), Traveling Magnetospheric Convection Twin Vortices: Another Case Study, Global Characteristics, and a Model, *Journal of Geophysical Research (Space Physics)*, *97*, doi:10.1029/91JA02464.

Hardy, D.A., M.S. Gussenhoven, R. Raistrick, and W.J. McNeil (1987), Statistical and functional representations of the pattern of auroral energy flux, number flux, and conductivity, *Journal of Geophysical Research*, *92*, 12275-12294, doi:10.1029/JA092iA11p12275.

Hartinger, M.D., D. Welling, N.M. Viall, M.B. Moldwin, and A. Ridley (2014), The effect of magnetopause motion on fast mode resonance, *Journal of Geophysical Research (Space Physics)*, *119*, 8212-8227, doi:10.1002/2014JA020401.

Hartinger, M.D., F. Plaschke, M.O. Archer, D.T. Welling, M.B. Moldwin, and A. Ridley (2015), The global structure and time evolution of dayside magnetopause surface eigenmodes, *Geophysical Research Letters*, *42*, 2594-2602, doi:10.1002/2015GL063623.

Kamide, Y., and S. Matsushita (1979), Simulation studies of ionospheric electric fields and currents in relation to field-aligned currents. I - Quiet periods., *Journal of Geophysical Research*, *84*, doi:10.1029/JA084iA08p04083.

Kim, H., X. Cai, C.R. Clauer, B.S. R. Kunduri, J. Matzka, C. Stolle, and D.R. Weimer (2013), Geomagnetic response to solar wind dynamic pressure impulse events at high-latitude conjugate points, *Journal of Geophysical Research (Space Physics)*, *118*, 6055-6071, doi:10.1002/jgra.50555.

Kim, H., C.R. Clauer, M.J. Engebretson, J. Matzka, D.G. Sibeck, H.J. Singer, C. Stolle, D.R. Weimer, Z. Xu (2015), Conjugate observations of traveling convection vortices associated with transient events at the magnetopause, *Journal of Geophysical Research (Space Physics)*, *120*, 2015-2035, doi:10.1002/2014JA020743.

Kivelson, M.G., and D.J. Southwood (1991), Ionospheric traveling vortex generation by solar wind buffeting of the magnetosphere, *Journal of Geophysical Research*, *96*, 1661-1667, doi:10.1029/90JA01805.

Kosch, M.J., M.W.J. Scourfield, and O. Amm (2000), The importance of conductivity gradients in ground-based field-aligned current studies, *Advances in Space Research*, *27*, 1277-1282, doi:10.1016/S0273-1177(01)00203-4.

Lam, M.M., and A.S. Rodger (2004), A test of the magnetospheric source of traveling convection vortices, *Journal of Geophysical Research (Space Physics)*, *109*, doi:10.1029/2003JA010214.

Lysak, R.-L. (1985), Auroral electrodynamics with current and voltage generators, *Journal of Geophysical Research*, *90*, 4178-4190, doi:10.1029/JA090iA05p04178.

Lysak, R.-L. (1990), Electrodynamic coupling of the magnetosphere and ionosphere, *Space Science Reviews*, *52*, 33-87, doi:10.1007/BF00704239.

McHenry, M.A., and C.R. Clauer (1987), Modeled ground magnetic signatures of flux transfer events, *Journal of Geophysical Research*, *92*, doi:10.1029/JA092iA10p11231.

Moretto, T., and A. Yahnin (1998), Mapping travelling convection vortex events with respect to energetic particle boundaries, *Annales Geophysicae*, *16*, doi:10.1007/s00585-998-0891-2.

Newell, P.T., and C.I. Meng (1989), Dipole tilt angle effects on the latitude of the cusp and cleft/low-latitude boundary layer, *Journal of Geophysical Research*, *94*, doi:10.1029/JA094iA06p06949.

Oguti, T. (1969), Conjugate Point Problems, *Space Science Reviews*, *9*, 745-804, doi:10.1007/BF00226262.

Oliveira, D.M. and J. Raeder (2014), Impact angle control of interplanetary shock geoeffectiveness, *Journal of Geophysical Research (Space Physics)*, *119*, doi:10.1002/2014JA020275.

Oliveira, D.M. and J. Raeder (2015), Impact angle control of interplanetary shock geoeffectiveness: A statistical study., *Journal of Geophysical Research (Space Physics)*, *120*, doi:10.1002/2015JA021147.

Powell, K.G., P.L. Roe, T.J. Linde, T.I. Gombosi, and D.L. De Zeeuw (1999), A solution-adaptive upwind scheme for ideal magnetohydrodynamics, *Journal of Computational Physics*, *154*, 284-209, doi:10.1006/jcph.1999.6299.

Pulkkinen, A., L. RastäTter, M. Kuznetsova, H. Singer, C. Balch, D. Weimer, G. Toth, A. Ridley, T. Gombosi, M. Wiltberger, J. Raeder, and R. Weigel (2013), Community-wide validation of geospace model ground magnetic field perturbation predictions to support model transition to operations, *Space Weather*, *11*, 369-385, doi:10.1002/swe.20056.

Ridley, A.J., and M.W. Liemohn (2002), A model-derived storm time asymmetric ring current driven electric field description, *Journal of Geophysical Research (Space Physics)*, *107*, 11151, doi:10.1029/2001JA000051.

Ridley, A, T. Gombosi, and D. De Zeeuw (2004), Ionospheric control of the magnetosphere: conductance, *Annales Geophysicae*, *22*, 567-584, doi:10.5194/angeo-22-567-2004.

Rosenberg, T.J., and J.H. Doolittle (1994), Studying the polar ionosphere and magnetosphere with Automatic Geophysical Observatories: The United States program in Antarctica, *Antarctic J. U.S.*, *29*, 347-349.

Shinbori, A., Y. Tsuji, T. Kikuchi, T. Araki, A. Ikeda, T. Uozumi, D. Baishev, B.M. Shevtsov, T. Nagatsuma, and K. Yumoto (2012), Magnetic local time and latitude dependence of amplitude of the main impulse (MI) of geomagnetic sudden commencements and its seasonal variation, *Journal of Geophysical Research*, *117*, doi:10.1029/2012JA018006.

Sibeck, D.G., R.A. Greenwald, W.A. Bristow, and G.I. Korotova (1996), Concerning possible effects of ionospheric conductivity upon the occurrence patterns of impulsive events in high-latitude ground magnetograms, *Journal of Geophysical Research*, *101*, 13407-13412, doi:10.1029/96JA00072.

Sibeck, D.G., N.B. Trivedi, E. Zesta, R.B. Decker, H.J. Singer, A. Szabo, H. Tachihara, and J. Watermann (2003), Pressure-pulse interaction with the magnetosphere and ionosphere, *Journal of Geophysical Research (Space Physics)*, *108*, 1095, doi:10.1029/2002JA009675.

Tóth, G., I.V. Sokolov, T.I. Gombosi, D.R. Chesney, C.R. Clauer, D.L. de Zeeuw, K.C. Hansen, K.J. Kane, W.B. Manchester, R.C. Oehmke, K.G. Powell, A.J. Ridley, I.I. Roussev, Q.F. Stout, O. Volberg, R.A. Wolf, S. Sazykin, A. Chan, B. Yu, and J. Kóta (2005), Space Weather Modeling Framework: A new tool for the space science community, *Journal of Geophysical Research (Space Physics)*, *110*A9, 12226, doi:10.1029/2005JA011126.

Weimer, D.R., D.M. Ober, N.C. Maynard, W.J. Burke, M.R. Collier, D.J. McComas, and T. Nagai (2002), Variable time delays in the propagation of the interplanetary magnetic field, *Journal of Geophysical Research*, *107*, doi:10.1029/2001JA009102.

Yu, Y.Q., and A.J. Ridley (2008), Validation of the space weather modeling framework using ground-based magnetometers, *Space Weather*, *6*, S05002, doi:10.1029/2007SW000345.

Yu, Y.Q., and A.J. Ridley (2009), The response of the magnetosphereionosphere system to a sudden dynamic pressure enhancement under southward IMF conditions, *Annales Geophysicae*, *27*, 4391-4407, doi:10.5194/angeo-27-4391-2009.

Yu, Y., A.J. Ridley, D.T. Welling, and G. Tóth (2010), Including gap region field-aligned currents and magnetospheric currents in the MHD calculation of ground-based magnetic field perturbations, *Journal of Geophysical Research (Space Physics)*, *115*, doi:10.1029/2009JA014869.

Yu, Y.Q., and A.J. Ridley (2011), Understanding the response of the ionosphereâĂŘmagnetosphere system to sudden solar wind density increases, *Journal of Geophysical Research (Space Physics)*, *116*, A04210, doi:10.1029/2010JA015871.

Yu, Y., V.K. Jordanova, A.J. Ridley, J.M. Albert, R.B. Horne, and C.A. Jeffrey (2016), A new ionospheric electron precipitation module coupled with RAM-SCB within the geospace general circulation model, *Journal of Geophysical Research (Space Physics)*, *121*, doi:10.1002/2016JA022585.

Figure 1.

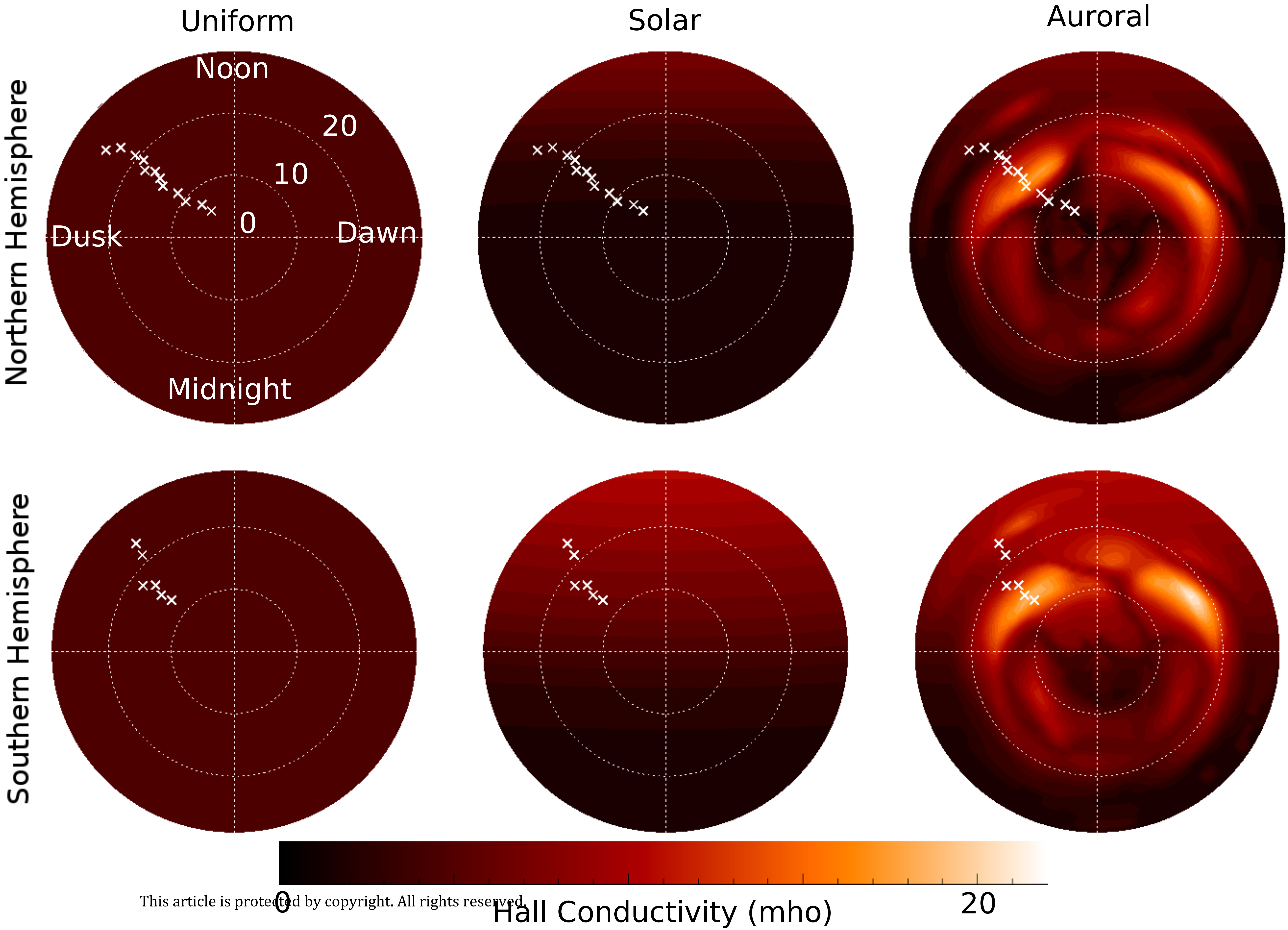
Uniform
Solar
Auroral
Northern Hemisphere
Southern Hemisphere
Noon
20
10
0
Dusk
Dawn
Midnight
0
20
Hall Conductivity (mho)

Figure 2.

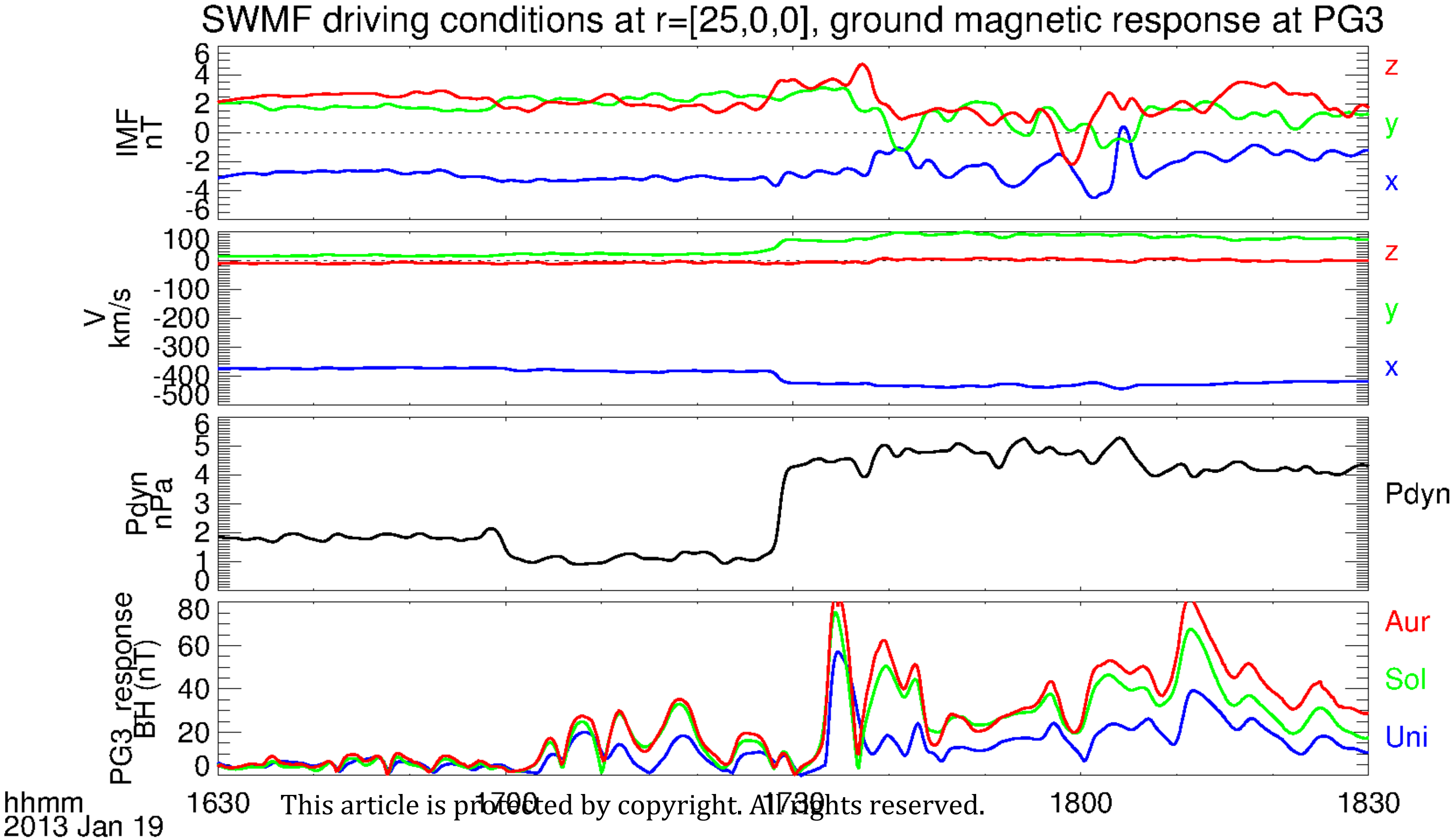
SWMF driving conditions at r=[25,0,0], ground magnetic response at PG3
IMF nT
z
y
x
V km/s
Pdyn nPa
Pdyn
PG3_response BH (nT)
Aur
Sol
Uni
hhmm
2013 Jan 19
1630
1700
1730
1800
1830

Figure 3.

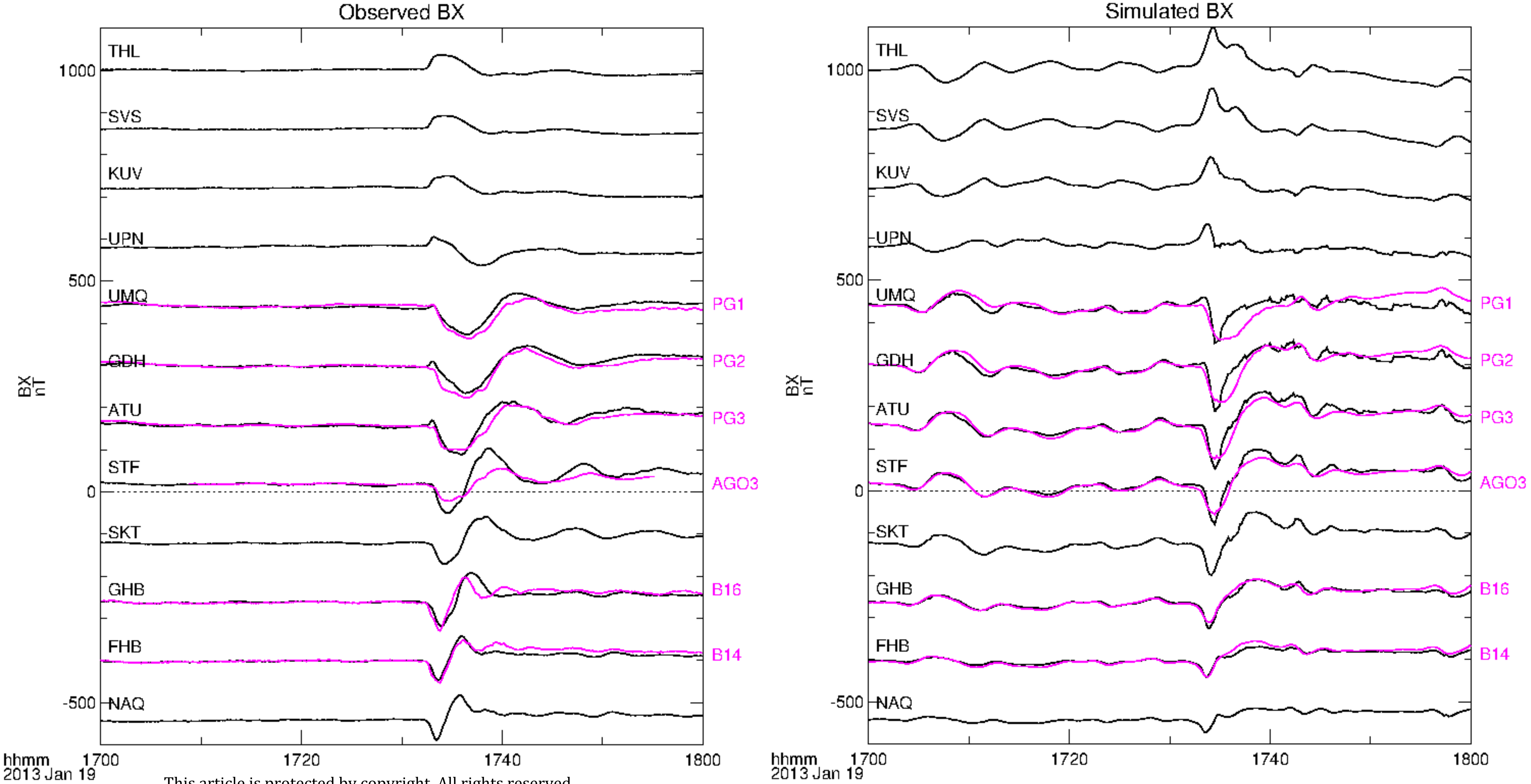

Observed BX
Simulated BX
THL
SVS
KUV
UPN
UMQ
GDH
ATU
STF
SKT
GHB
FHB
NAQ
PG1
PG2
PG3
AGO3
B16
B14
BX
nT
1000
500
0
-500
hhmm
2013 Jan 19
1700
1720
1740
1800

Figure 4.

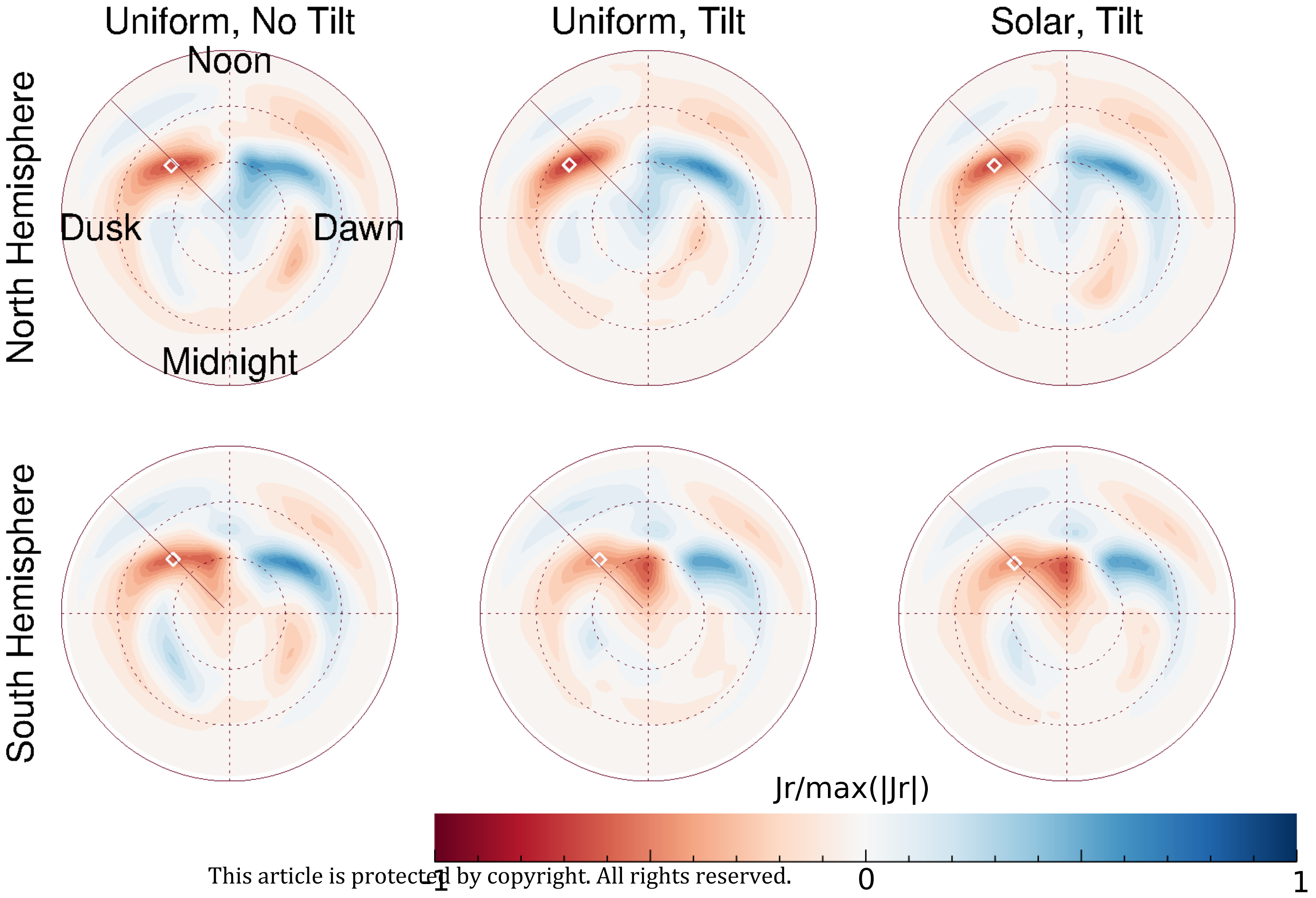

Uniform, No Tilt
Uniform, Tilt
Solar, Tilt
Auroral, Tilt
Noon
Dusk
Dawn
Midnight
North Hemisphere
South Hemisphere
Jr/max(|Jr|)
-1
0
1

Figure 5.

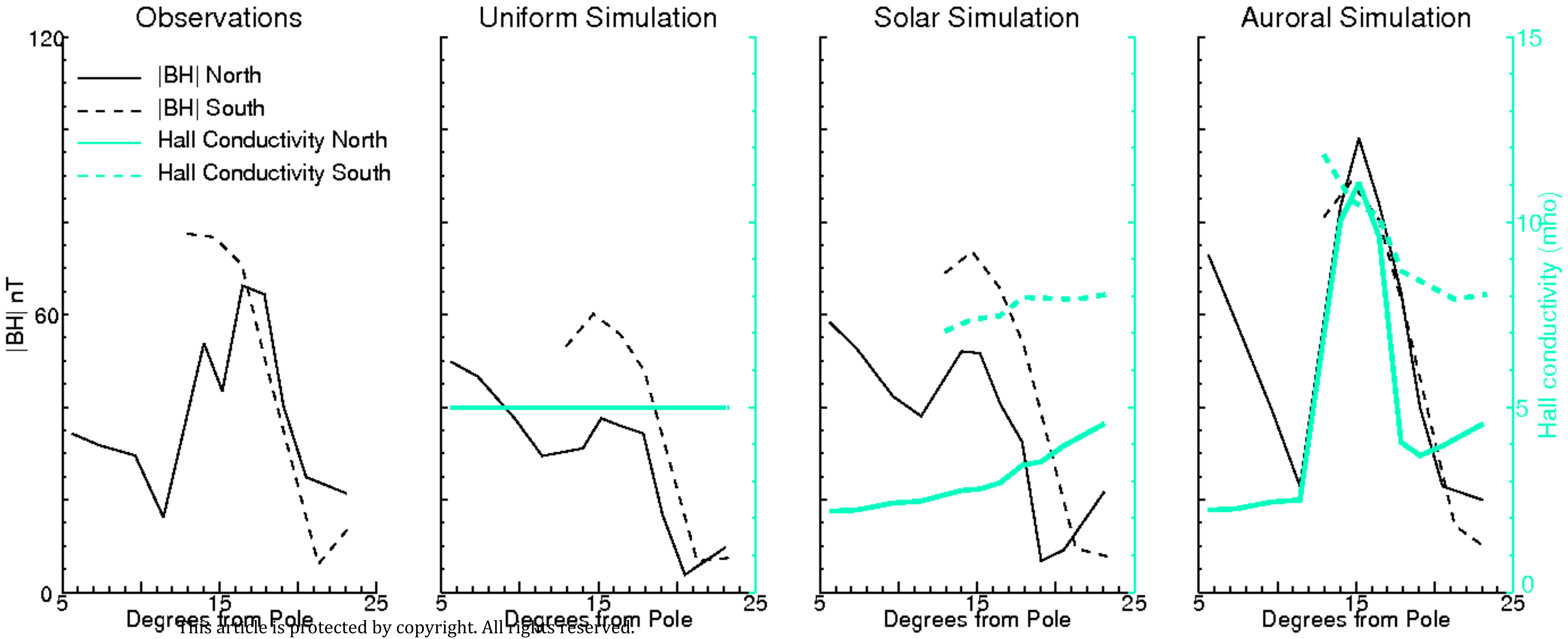

Observations
Uniform Simulation
Solar Simulation
Auroral Simulation
|BH| North
|BH| South
Hall Conductivity North
Hall Conductivity South
|BH| nT
Hall conductivity (mho)
120
60
0
15
10
5
0
5
15
25
Degrees from Pole

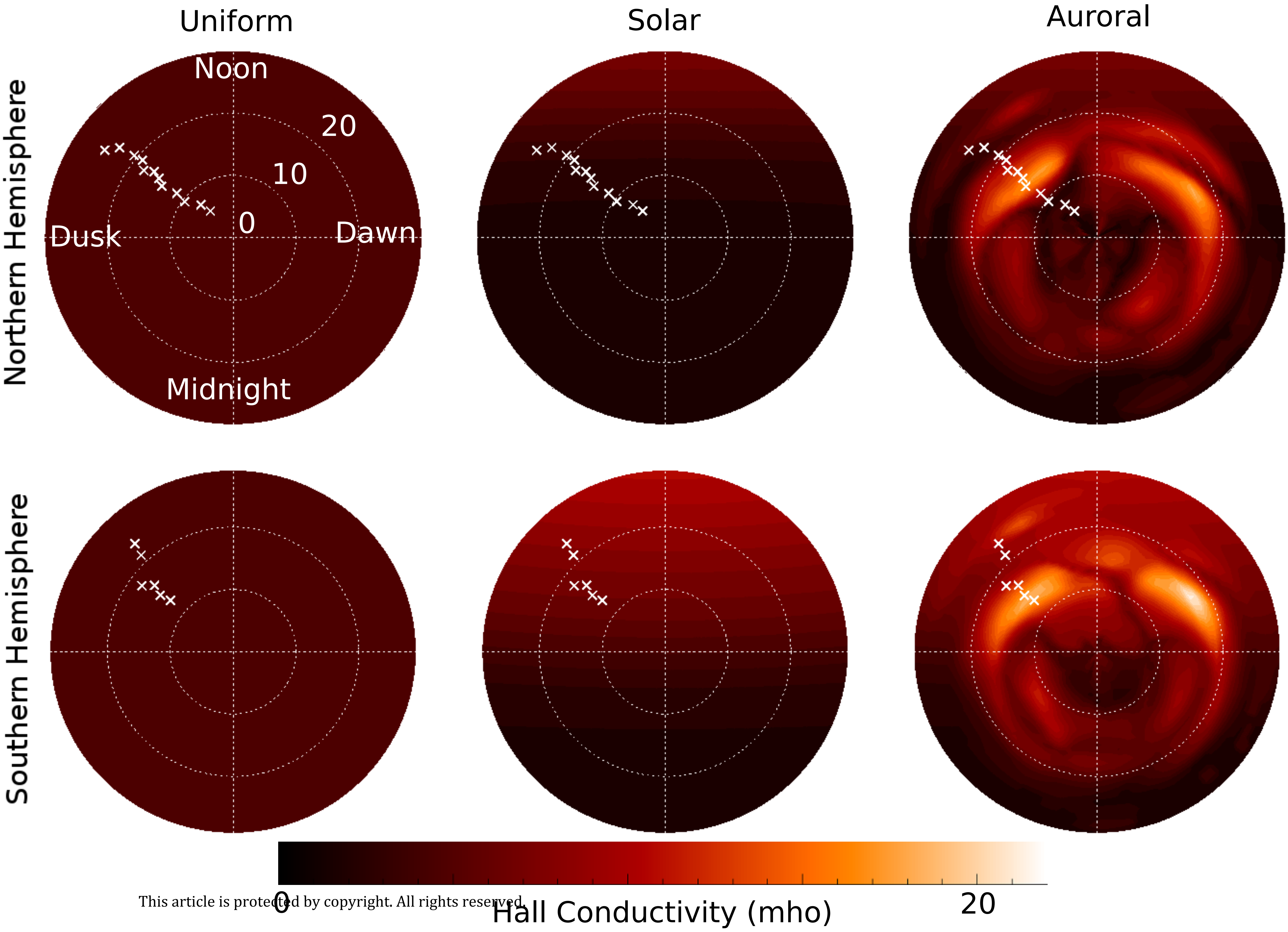

Uniform
Solar
Auroral
Northern Hemisphere
Southern Hemisphere
Noon
Dusk
Dawn
Midnight
0
10
20
0
20
Hall Conductivity (mho)

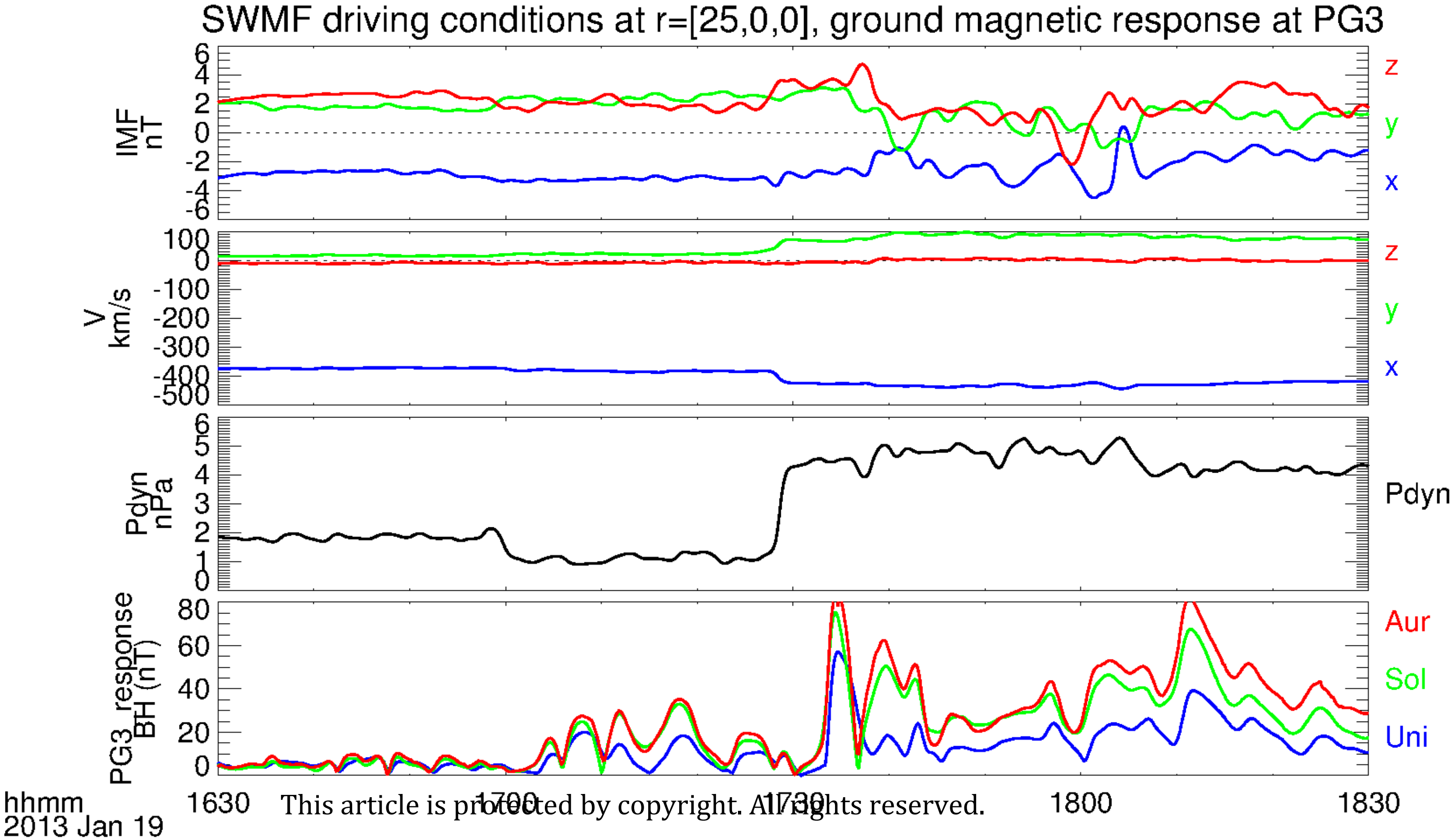

SWMF driving conditions at r=[25,0,0], ground magnetic response at PG3
IMF
nT
6
4
2
0
-2
-4
-6
z
y
x
V
km/s
100
0
-100
-200
-300
-400
-500
z
y
x
Pdyn
nPa
6
5
4
3
2
1
0
Pdyn
PG3_response
BH (nT)
80
60
40
20
0
Aur
Sol
Uni
hhmm
2013 Jan 19
1630
1700
1730
1800
1830

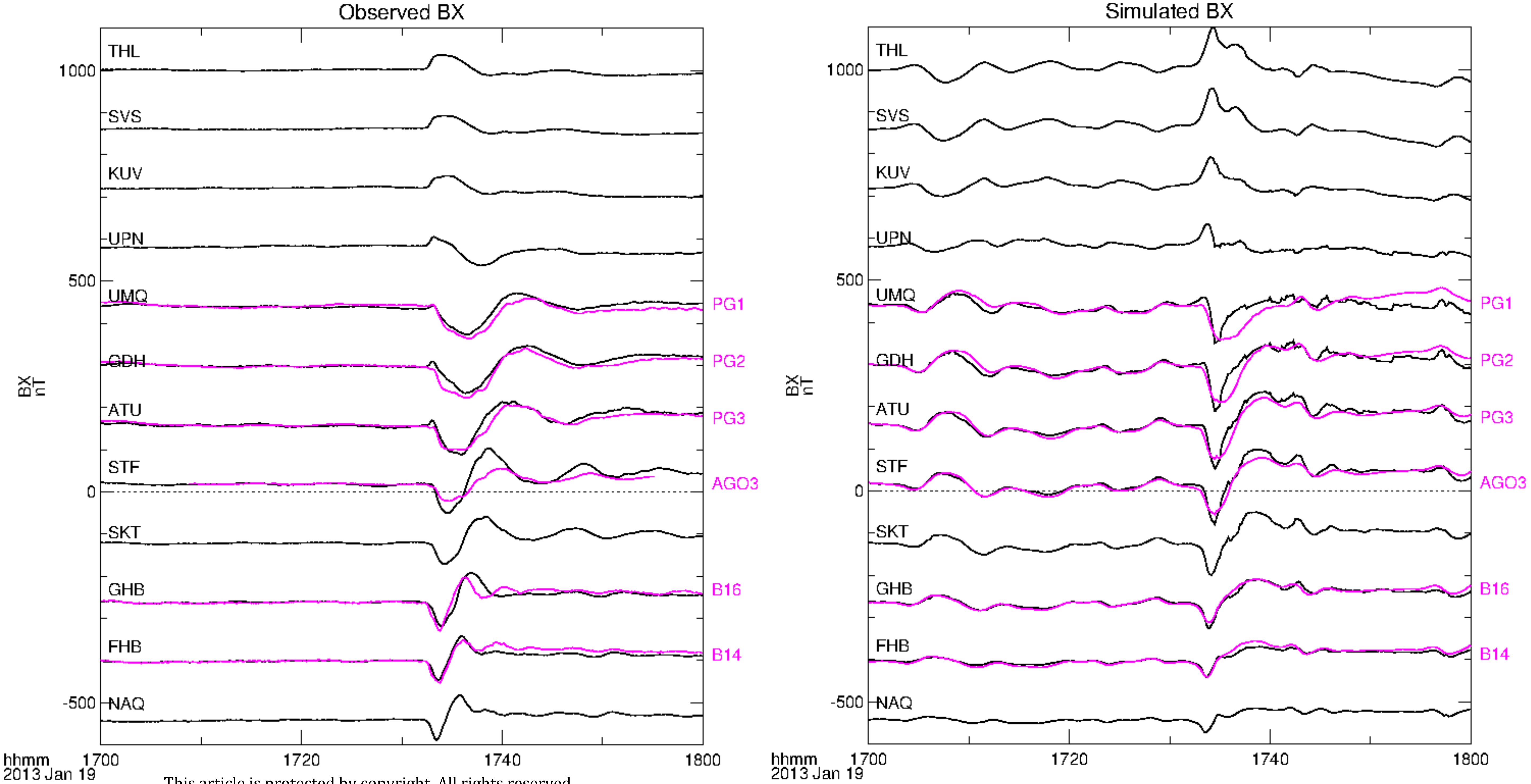

Observed BX
Simulated BX
THL
SVS
KUV
UPN
UMQ
GDH
ATU
STF
SKT
GHB
FHB
NAQ
PG1
PG2
PG3
AGO3
B16
B14
BX nT
1000
500
0
-500
hhmm 2013 Jan 19
1700
1720
1740
1800

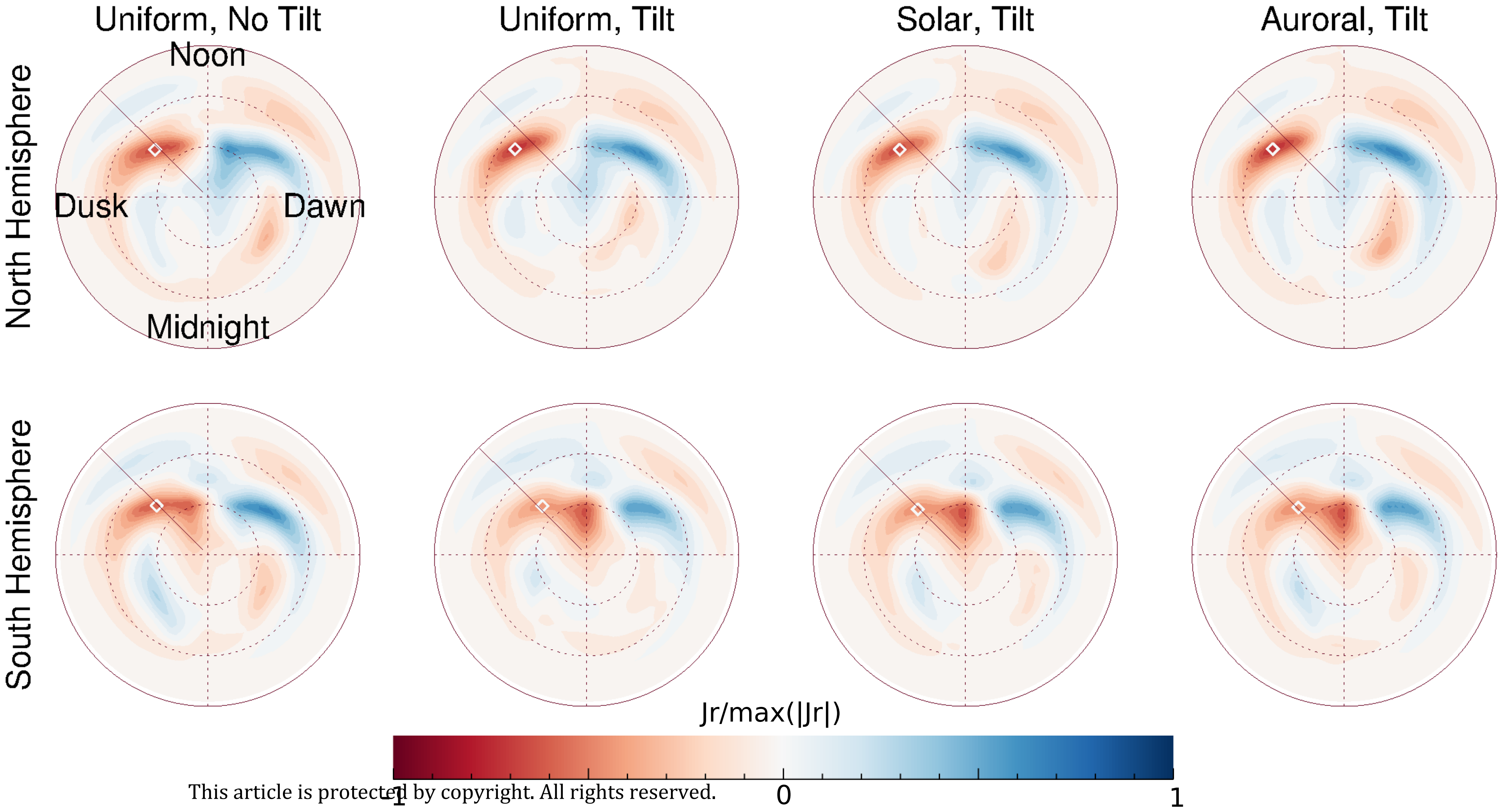

Uniform, No Tilt
Uniform, Tilt
Solar, Tilt
Auroral, Tilt
Noon
Dusk
Dawn
Midnight
North Hemisphere
South Hemisphere
Jr/max(|Jr|)
-1
0
1

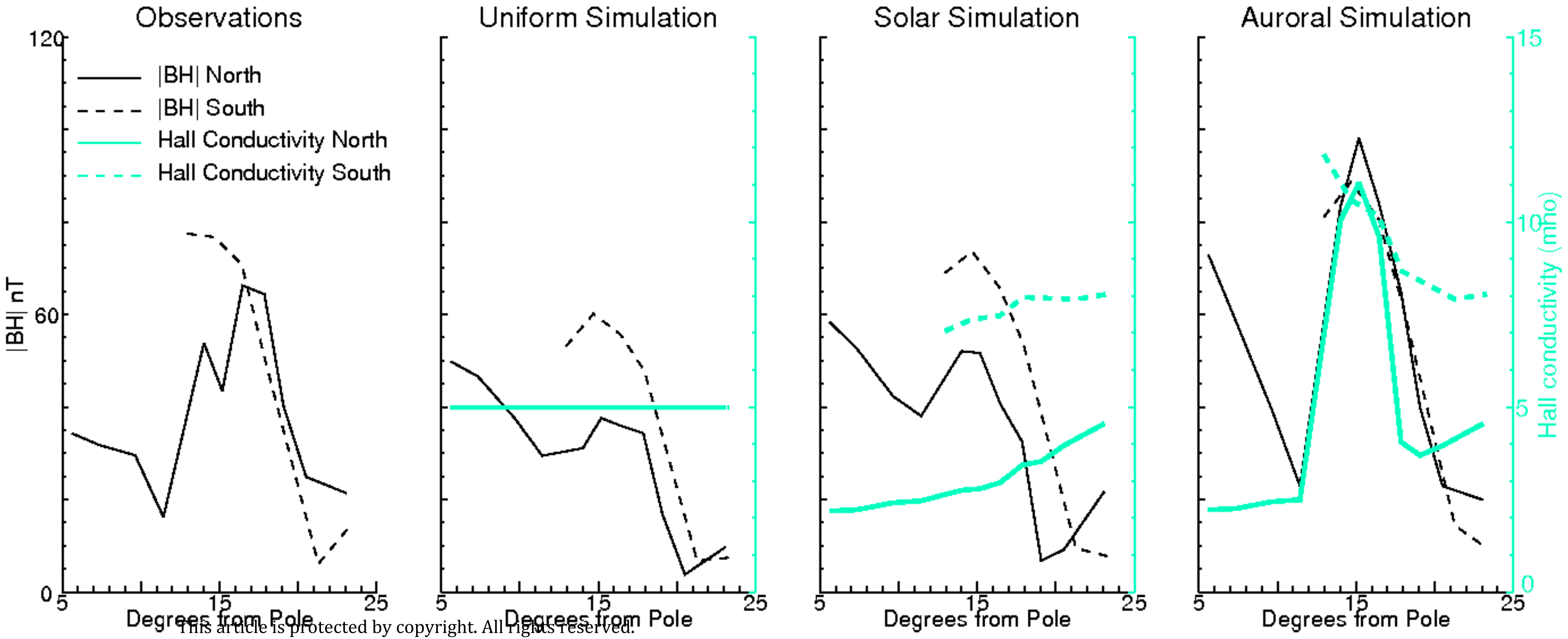
Observations
Uniform Simulation
Solar Simulation
Auroral Simulation
|BH| North
|BH| South
Hall Conductivity North
Hall Conductivity South
|BH| nT
120
60
0
5
15
25
Degrees from Pole
Hall conductivity (mho)
15
10
5
0